Supporting Information

Faceting-Controlled Zeeman Splitting in Plasmonic TiO_2 Nanocrystals

*Penghui Yin, Manu Hegde, Natalie S. Garnet, Yi Tan, and Pavle V. Radovanovic**

Department of Chemistry University of Waterloo, 200 University Avenue West, Waterloo, Ontario N2L 3G1, Canada

*Corresponding author (Email: pavler@uwaterloo.ca)

Table of Contents

Experimental Methods……...S2

Supporting Figures…….....S8

Supporting Text……S22

Supporting References……..S27

EXPERIMENTAL METHODS

Materials. Titanium(IV) fluoride (TiF_4), titanium(IV) chloride ($TiCl_4$, 99.9%), oleic acid (OLAC, 90%), 1-octadecence (ODE, 90%), oleylamine (OLAM, 70%), and 1-octadecanol (ODOL, 95%) were purchased from Sigma Aldrich. All the chemicals are used without further purification.

Synthesis of TiO_2 NCs. The TiO_2 NCs were synthesized using a modified procedure based on the seeded growth method developed by Gordon *et al*.[S1] In a typical synthesis, precursor solution was prepared by dissolving 2 mmol titanium halide (TiF_4 (F), $TiCl_4$ (Cl), or their 1:1 mixture (M)) together with 10 mmol OLAC in 6.8 mL ODE in a glove box. The synthesis was conducted under argon atmosphere using a Schlenk line. In a separate 100 mL three-neck round bottom flask, 30 mmol coordinating ligand (OLAM or ODOL) was mixed with 0.48 mL OLAC and 10.2 mL ODE. The mixture was degassed by heating to 120 °C within 20 minutes and keeping it at that temperature for 1 hour. After degassing, the mixture was cooled to 60 °C before injecting 1.5 mL titanium halide precursor solution. The mixture was then quickly heated to 290 °C and held for 10 min for the crystal seeds to nucleate. The remaining 8.5 mL titanium halide solution was injected into the flask at the rate of about 0.3 mL/min at 290 °C. After that, the mixture was allowed to cool down to room temperature naturally. The product was collected by centrifugation at 3000 rpm for 5 min and redispersed in a small amount of toluene. To purify the product, NCs were precipitated by adding ethanol to the suspension. The washing was repeated three times and the NCs were finally dispersed in hexane, toluene, or chloroform for further

characterizations. For notation of different samples, we adopted the designation previously used for these samples, which specifies the precursor and coordinating ligand using the following abbreviations: F-OLAM, M-OLAM, and Cl-ODOL.

Characterization and Measurements. Powder X-ray diffraction (XRD) patterns were recorded using an INEL diffractometer with a position-sensitive detector and monochromatic Cu Kα radiation (λ = 1.5418 Å). Powder samples were obtained by precipitating the NCs in chloroform suspension by the addition of ethanol and subsequent centrifugation. Transmission electron microscopy images were collected with a JEOL-2010F microscope operating at 200 kV. The specimens for TEM measurements were prepared by drop casting diluted colloidal suspensions in toluene on copper grids with lacey Formvar/carbon support films purchased from Ted Pella, Inc. The nanocrystal sizes were analyzed by dynamic light scattering. Dynamic light scattering measurements were performed at 25 °C by utilizing a Zetasizer Nano-S90 system (Malvern Instruments) with a laser wavelength of 633 nm positioned at the fixed angle of 90 degrees. The absorption spectra were collected with a Varian Cary 5000 UV-vis-NIR spectrophotometer. The UV-vis absorption measurements were made on NC suspensions in hexane, and NIR absorption spectra were collected upon drop-casting the NC suspensions in chloroform onto quartz substrates. Fourier transform infrared (FTIR) spectra were recorded using a FTIR Bruker Tensor 37 spectrometer. Powder samples were mixed with KBr in approximately 1:50 weight ratio and pressed into pellets for the FTIR measurement. X-ray photoelectron spectroscopy measurements were performed using a Thermo-VG Scientific ESCALab 250 microprobe equipped with a monochromatic Al Kα radiation source (1486.6 eV). Powder

samples for XPS measurements were prepared in the same way as for XRD measurements. Titanium K-edge XANES spectra were collected at the 20-BM beamline of the Advanced Photon Source (APS). A titanium foil was used to internally calibrate the energy of the Ti K-edge (6966 eV). The spectra were collected in transmission mode using a gaseous ionization detector filled with nitrogen.

Magnetic circular dichroism measurements were carried out in Faraday configuration using a Jasco J-815 spectropolarimeter.[S2] Samples were housed in an Oxford SM 4000 magneto-optical cryostat which allows for variable-temperature (1.5 to 300 K) and variable-field (0 to 7 T) operation. For sample preparation, a colloidal NC suspension in chloroform was drop-casted onto strain-free quartz substrate and dried in the air. Magnetic-field-dependent MCD measurements were made at magnetic fields from 0 to 7 T in 1 T interval. The variable-temperature MCD spectra were collected at 7 T and different temperatures (5, 10, 20, 50, 100, 200, and 300 K). Magnetization measurements were performed using a Physical Property Measurement System (PPMS, Quantum Design Model 6000). For the measurement of free-standing NCs, the colloids were precipitated with ethanol, dried, and loaded into the sample capsules. The measurements were made at 2 K with magnetic field ranging from 0 to 9 T. Electron paramagnetic resonance spectra were collected for powder samples using a Bruker X-band EMXmicro spectrometer equipped with EMX standard resonator and ESR900 continuous flow cryostat (Oxford Instruments) for temperature control. The EPR spectra were obtained at 80 K with the incident microwave frequency of 9.39 GHz, power of 0.63 mW, and modulation amplitude of 4 Gauss by averaging 4 scans.

Spectral Analysis. The XPS spectra were calibrated against the C 1s peak (284.8 eV) of adventitious carbon. Voigt functions and Shirley backgrounds were used for fitting the Ti 2p spectra. Ti K-edge X-ray absorption spectra were normalized to the EXAFS region. Peak deconvolution was performed for the spectral range from 4965 to 4988 eV using Voigt functions and a constant background.

MCD spectra were analysed as described elsewhere.[S2,S3] MCD spectra collected at different magnetic fields were background-corrected by subtraction of the spectrum collected at 0 T under identical temperature. Using the baseline-corrected MCD spectra, the intensities of the specific transitions were determined by integrating the area under the corresponding MCD signal. For deconvolution of the MCD peaks of M-OLAM sample, a Voigt function was used to fit the 7 T MCD spectrum collected at 300 K to obtain the peak profile for the excitonic transition. The peak position and band width obtained from this fitting were kept unchanged for fitting the spectra at different magnetic field strengths and temperatures. The second Voigt function was added to achieve the best fitting of the negative band in the range from 2.26 to 4.5 eV. Practically unchanged peak position and band width of the second Voigt function indicated that peak devolution was reasonable. The different profile of the deconvoluted peaks can be attributed to different characteristics of the excitonic and charge transfer transitions.

The magnetic field dependence of the MCD band intensity was fitted to a linear function, spin-only Brillouin function (equation 2), or the linear combination of the two functional forms, as described in the main text. For fitting of temperature-dependent MCD intensities, the integrated intensity at 300 K was taken as the A term MCD contribution and subtracted from the MCD intensities at all other temperatures to obtain the temperature dependence

of the MCD C term. The C term MCD intensities were fitted to the Curie-Weiss law (equation 1). Adding A term MCD intensity (300 K) to the fitted curve for C term intensity reproduces the temperature dependence of the overall MCD intensity. For comparison of the MCD spectra of different TiO_2 samples, the MCD intensities were converted to $\Delta A/A$ from ellipticity (θ) using the relationship:

$$\frac{\Delta A}{A} = \frac{\theta}{32982 \times A} \qquad \text{(S1)}$$

where θ is in millidegree, and A is the band gap absorbance determined from the absorption spectrum simultaneously collected by the CD detector.

For the analysis of EPR spectrum of M-OLAM sample, a Lorentzian function (red dashed line in Figure S13a) was used to simulate the broad background associated with mutually interacting Ti^{3+} ions, and subtracted from the spectrum to obtain the EPR signal associated with isolated Ti^{3+} ions (blue dashed line in Figure S13a).

Computational Method. The electronic structure of oxygen vacancies in anatase TiO_2 was simulated using the plane-wave density functional theory within GGA+U (Hubbard U correction) approximation as developed in Quantum-ESPRESSO package.[S4] The anatase TiO_2 supercell of 108 atoms (3×3×1) was constructed for the calculations. Norm-conserving pseudopotential along with U-corrected PBE exchange-correlation functional with plane-wave cutoff energy of 80 Ry was used in calculations.[S5] The Hubbard U correction of 3.2 eV on Ti 3d electrons and 2.0 eV on O 2p electrons were used to overcome strong Ti 3d and O 2p coupling.[S6] The 108 atoms supercell was relaxed in such a way that total force on each atom is less than 10^{-3} Ry/a.u. and total energy of the system less than 10^{-4} Ry. The O vacancy was created by removing one of the oxygen atoms from the

supercell. For geometrical optimization total energy was calculated using 1×1×1 Monkhorst-Pack (MP) k-point mesh (from Γ point). The equilibrium lattice parameters obtained from the geometrical optimization procedure were used for further calculations. For self-consistent and non-self-consistent calculations, a denser MP grid of 2×2×2 was used.

SUPPORTING FIGURES

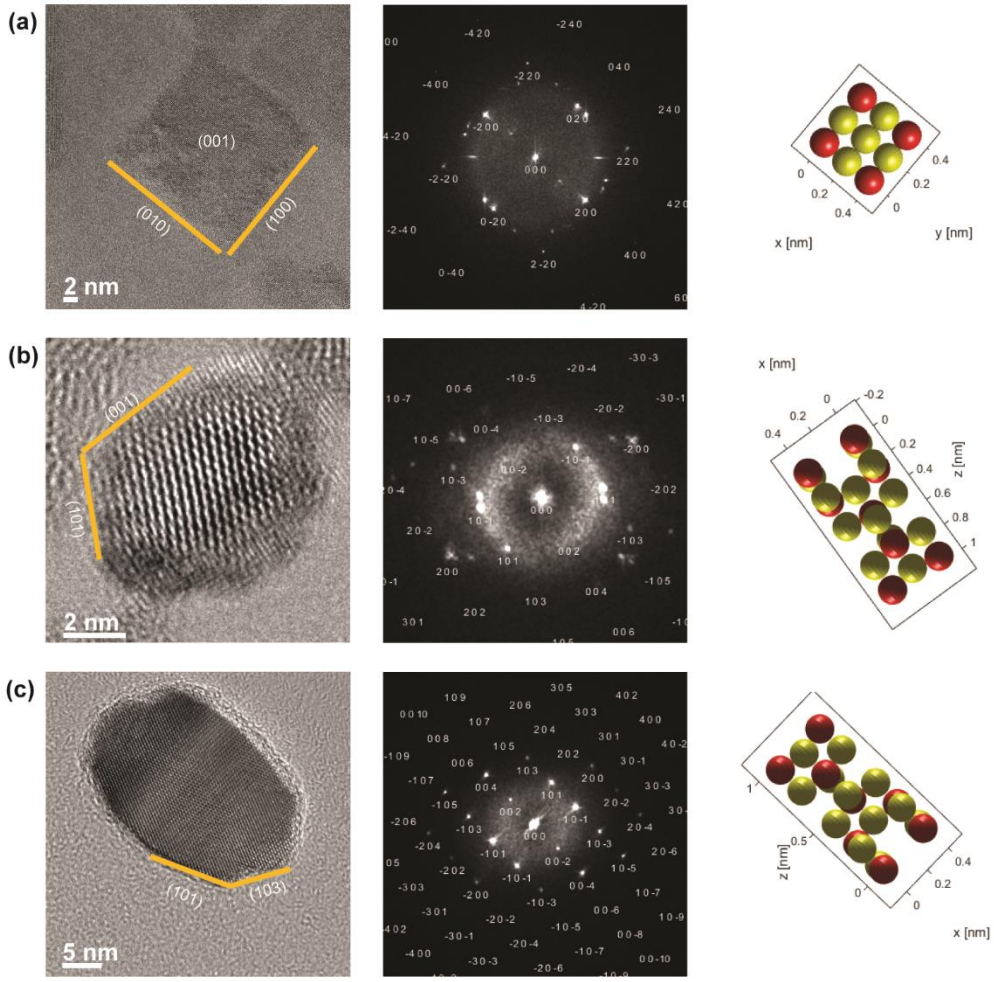

Figure S1. Lattice-resolved TEM images (left panels), their Fourier transform (middle panels), and atomic simulation of the corresponding crystal lattice orientation (right panels) for (a) F-OLAM NCs, (b) M-OLAM NCs, and (c) Cl-ODOL NCs. Orange lines in TEM images designate the lattice planes, as indicated. Red spheres in right hand side panels indicate titanium and yellow spheres oxygen atoms.

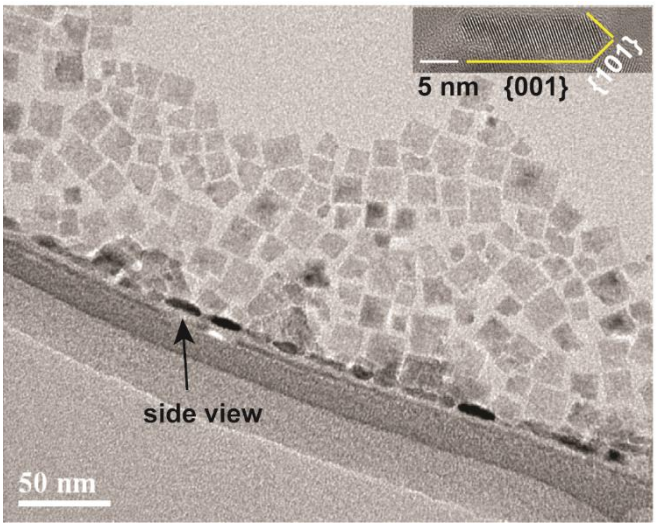

Figure S2. Overview TEM image of F-OLAM NCs showing different NC orientations. Side view of a typical nanoplatelet oriented perpendicular to the square base is indicated with an arrow. Inset: high-resolution TEM image of a nanoplatelet oriented perpendicular to the square base, indicating relevant lattice planes.

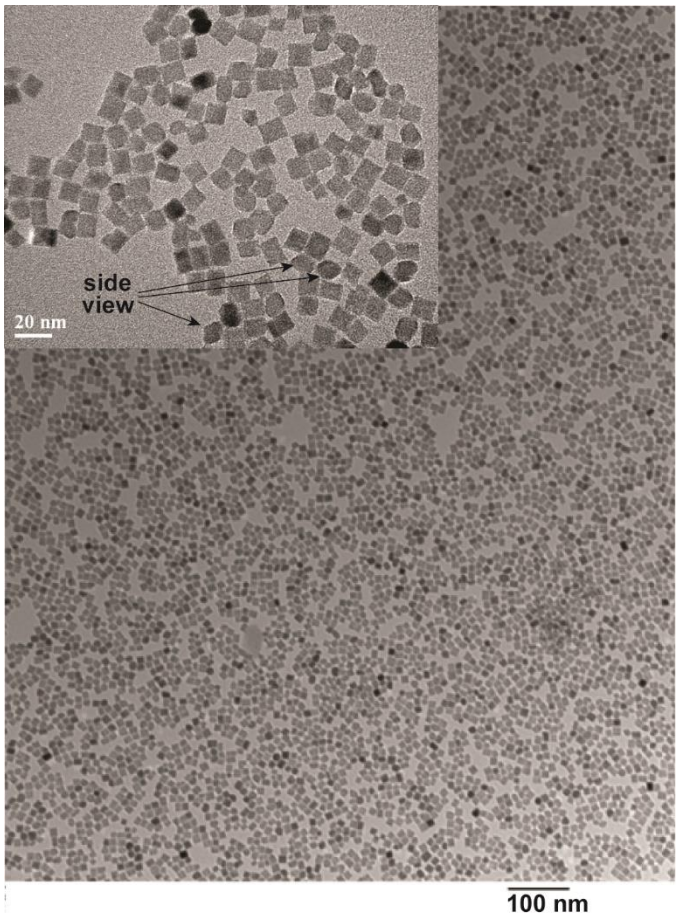

Figure S3. Overview TEM image of M-OLAM NCs showing NC uniformity throughout the sample. Inset: zoom-in of the overview image showing different NC orientations. Typical truncated square bipyramidal NCs oriented perpendicular to the square base are indicated with an arrow. High-resolution TEM of a M-OLAM NC oriented perpendicular to the NC square base is shown in Figure 1b (middle). Additional discussion about NC faceting, including the difference between F-OLAM and M-OLAM NCs is given in Supporting Text on pages S23-S25.

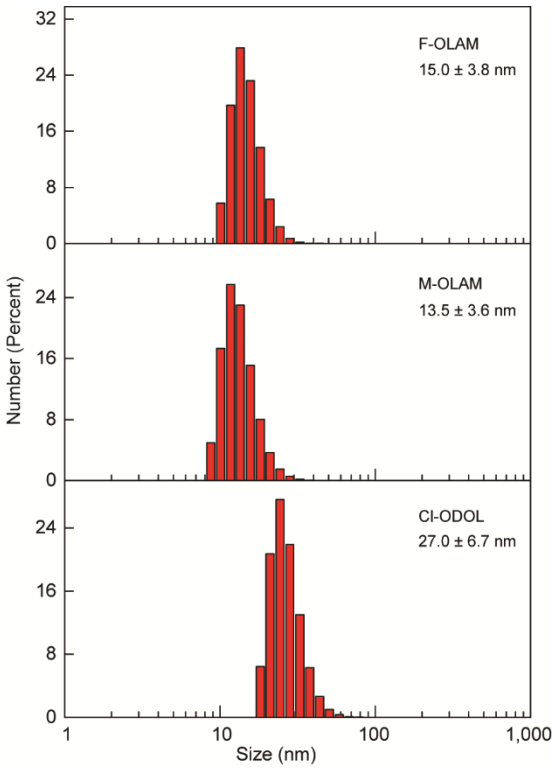

Figure S4. Size distribution histograms for F-OLAM (top), M-OLAM (middle) and Cl-ODOL (bottom) TiO_2 nanocrystals determined from dynamic light scattering measurements on toluene suspensions. The average nanocrystal sizes and standard deviations are shown in the corresponding graphs.

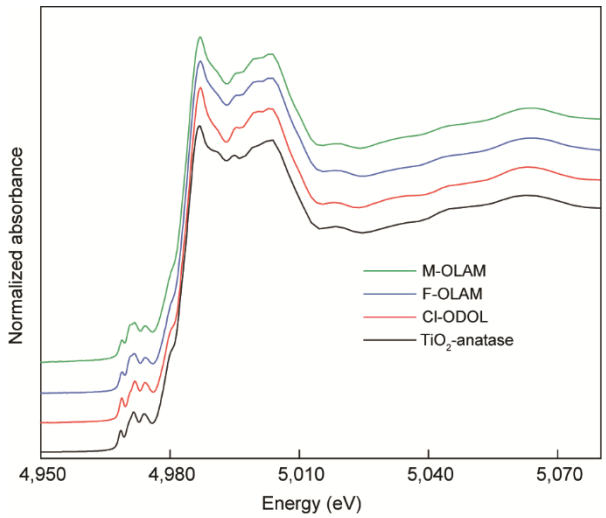

Figure S5. Overview XANES spectra of F-OLAM, M-OLAM, and Cl-ODOL nanocrystal samples, as indicated in the graph. Spectrum of commercial anatase TiO_2 powder (black trace) is shown for comparison.

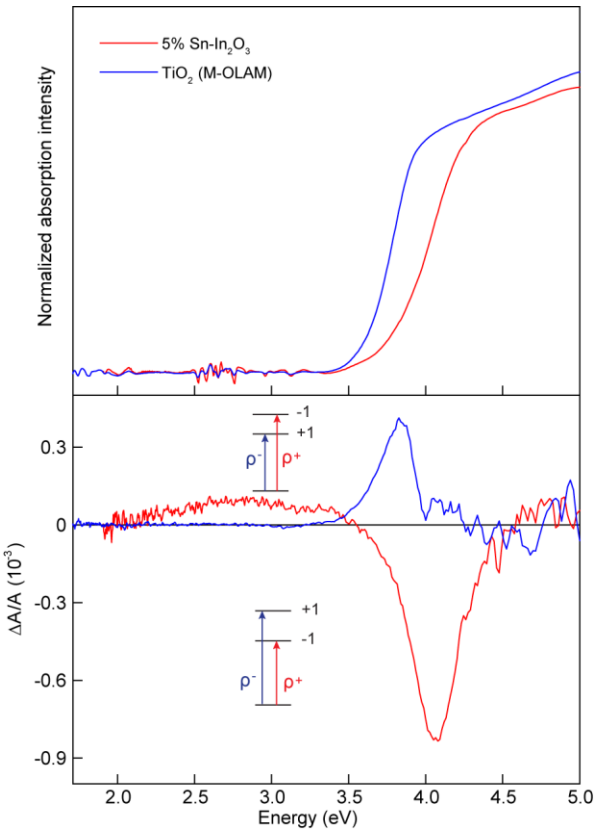

Figure S6. Comparison between 300 K MCD spectra of M-OLAM TiO_2 and 5 % Sn-doped In_2O_3 (ITO) nanocrystals. The opposite sign of MCD bands attests to the role of the nanocrystal electronic structure on the magnetoplasmon-induced excitonic splitting (illustrated in the insets).

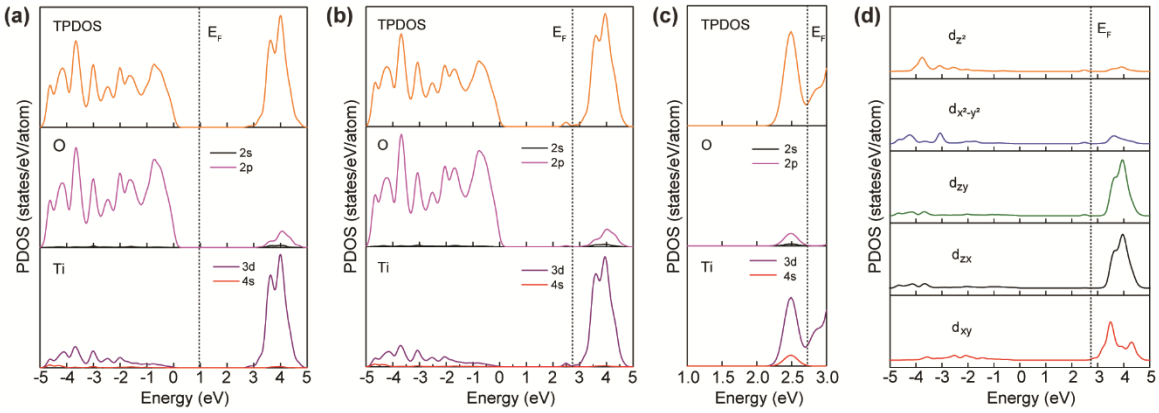

Figure S7. Density functional theory calculations for TiO_2 nanocrystals. (a-c) Projected density of states for Ti (bottom panels) and O (middle panels), and total projected density of states (top panels) for (a) ideal TiO_2 supercell, (b) vacancy-containing TiO_2 supercell, and (c) vacancy-containing TiO_2 supercell near the conduction band edge. The Fermi levels are shown with dashed lines. The valence and conduction bands have mostly oxygen 2p and titanium 3d character, respectively (see more detailed discussion in the Supporting Text section). (d) Titanium d-orbital contribution to the Ti projected density of states, indicating that the lower part of the conduction band is dominated by d_{xy} orbitals.

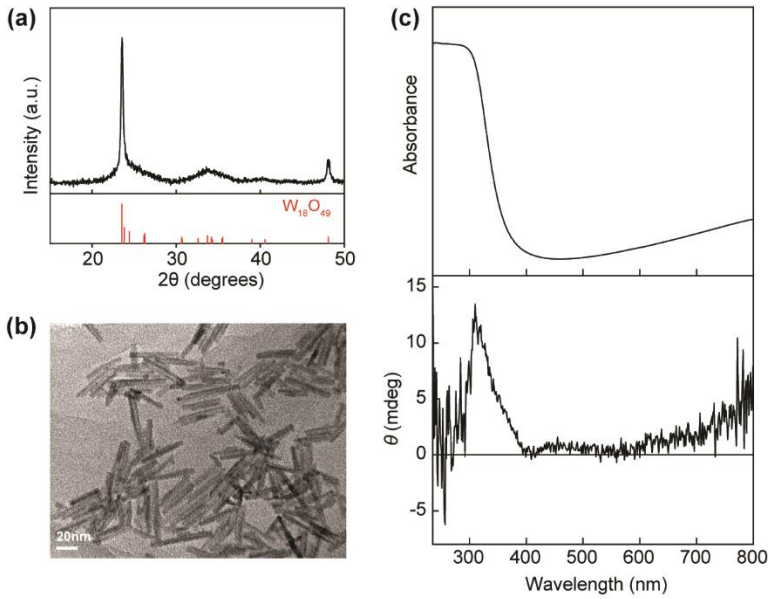

Figure S8. Characterization and magneto-optical properties of $WO_{2.72}$ nanocrystals. (a) XRD pattern of $WO_{2.72}$ nanocrystals, prepared by modifying a procedure used for the synthesis of tungsten nanoparticles.[S7] The XRD pattern of the nanocrystal sample agrees well with that reported for $WO_{2.72}$ phase (red sticks, JCPDS-084-1516). (b) TEM image of $WO_{2.72}$ sample in (a) demonstrating the formation of nanorods. (c) 300 K absorption (top panel) and MCD (bottom panel) spectra of the same $WO_{2.72}$ nanorods. In addition to the excitonic absorption with the onset at ca. 400 nm, a broad feature extending into near-IR range corresponds to LSPR, consistent with the previously reported results for similar nanocrystals. Importantly, a positive sign of the excitonic MCD band with the maximum at ca. 300 nm is observed, similar to TiO_2 nanocrystals.

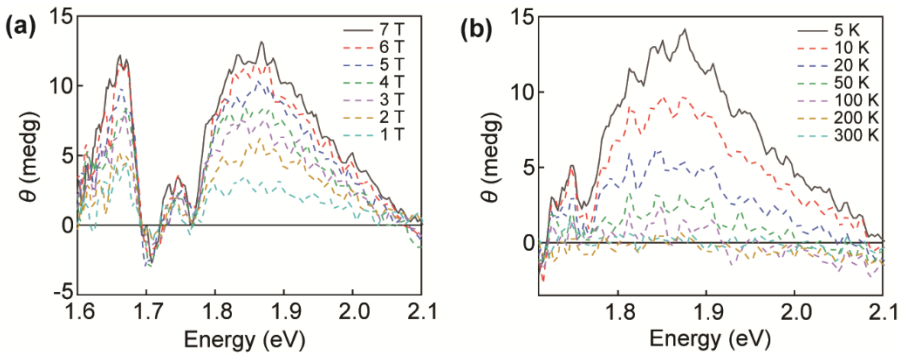

Figure S9. Ligand-field MCD spectra of M-OLAM TiO_2 NCs in the low-energy region, assigned to symmetry-split $^2T_2 \rightarrow {}^2E$ transitions characteristic for six-coordinate Ti^{3+}. (a) Variable-magnetic-field MCD spectra showing saturation behaviour of MCD intensity with increasing magnetic field strength. (b) Variable-temperature MCD spectra showing decreased intensity with increasing temperature. Both magnetic field and temperature dependencies are consistent with paramagnetic behavior, as discussed in the main text.

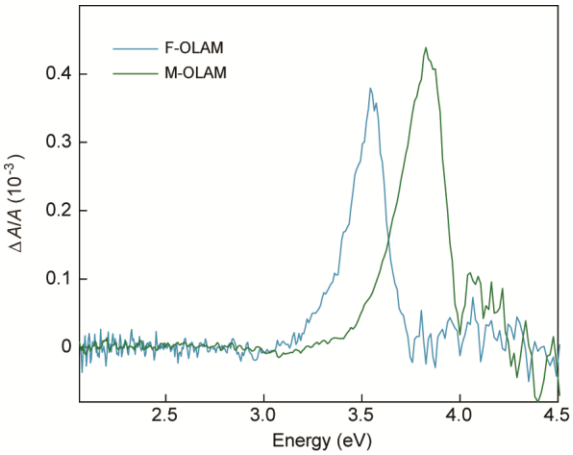

Figure S10. 300 K MCD spectra of F-OLAM (blue trace) and M-OLAM (green trace) nanocrystals in the band gap region. The MCD intensities are shown normalized to band edge absorbance ($\Delta A/A$), and thus are directly comparable.

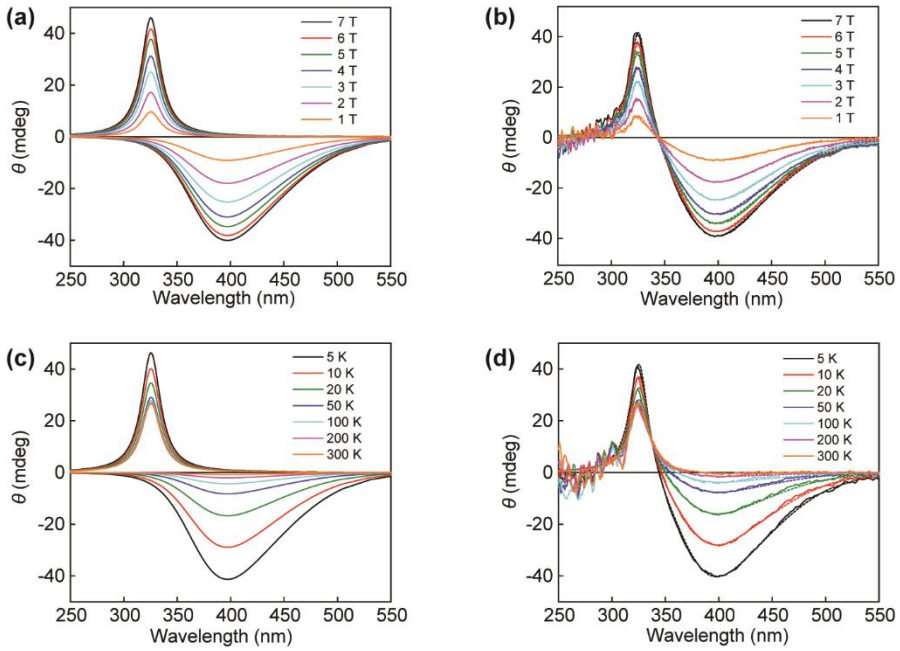

Figure S11. (a) Deconvoluted bands for charge transfer transition (negative band) and excitonic transition (positive band) for different magnetic field strengths. (b) Best overall fits (dashed lines) to the experimental spectra (solid lines) for different magnetic field strengths. (c) Deconvoluted bands for charge transfer transition and excitonic transition for different temperatures. (d) Best overall fits (dashed lines) to the experimental spectra (solid lines) for different temperatures. The overall fits are in excellent agreement with the experimental spectra in both (b) and (d).

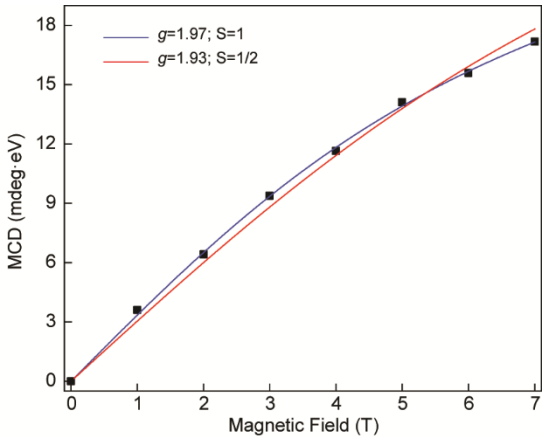

Figure S12. Magnetic field dependence of the integrated excitonic MCD intensity for M-OLAM TiO_2 nanocrystal sample (black squares). Solid lines are best fits involving a combination of linear dependence (representing the magnetoplasmon-induced splitting) and Brillouin function (blue line corresponds to g=1.97 and S=1, and red line to g=1.93 and S=1/2). The best agreement is obtained for high net spin state (S=1).

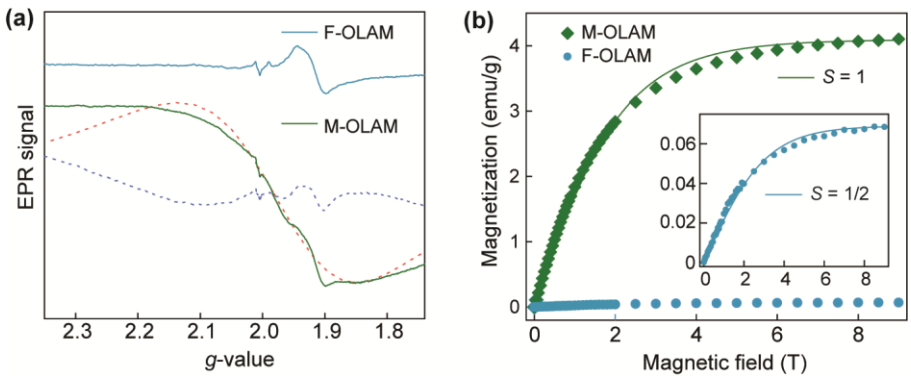

Figure S13. (a) EPR spectra of F-OLAM (blue trace) and M-OLAM (green trace) nanocrystal samples. Red dashed line represents the Lorentzian fit to the broad signal arising from strongly interacting internal Ti^{3+}, and dashed dark blue line is a spectrum of M-OLAM sample upon subtraction of the Lorentzian fitting curve. (b) Magnetization as a function of applied magnetic field for F-OLAM and M-OLAM nanocrystal samples. Best fits of the Brillouin function (equation 2 in the main text) to the experimental data are shown by corresponding lines. Based on the MCD and EPR results the fitting was performed using S=1/2 and g=1.93 for F-OLAM, and S=1 and g=1.97 for M-OLAM nanocrystals. Inset shows zoomed-in data for F-OLAM sample (a relatively small deviation from ideal S=1/2 behavior is due to coupling with the residual orbital magnetic moment associated with the Ti^{3+} site symmetry).

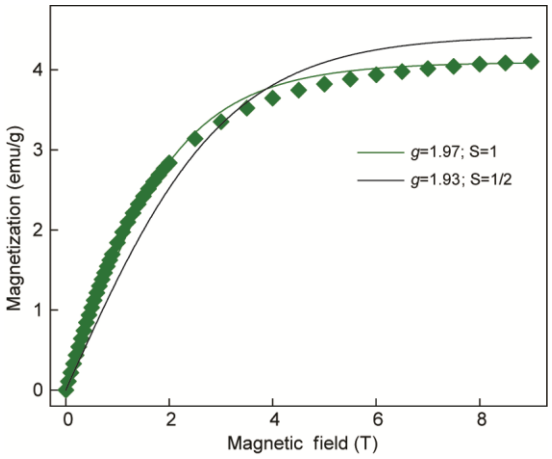

Figure S14. Comparison between the Brillouin fits (solid lines) to the experimental magnetization data for M-OLAM sample (green diamonds) for *S*=1/2 (black line) and *S*=1 (green line). The *g*-values used for fitting are the characteristic values for different Ti^{3+} species, as discussed in the main text. The best agreement between the fit and the experimental data is obtained for high spin state (*S*=1), which corresponds to Ti^{3+} exchange-coupled pairs. Minor deviation of the experimental data points from the *S*=1 Brillouin fit can be associated with the presence of a small fraction isolated Ti^{3+} (*S*=1/2).

SUPPORTING TEXT

Magnetic Circular Dichroism of LSPR. Magnetic circular dichroism (MCD) of LSPR has been associated with the formation of cyclotron magnetoplasmonic modes, as discussed in ref. 24 in the main text. Briefly, when excited by circularly polarized light, cyclotron LSPR modes are generated, with the rotation direction determined by the light polarization. In the absence of an external magnetic field, the two cyclotron plasmonic modes, corresponding to excitation by left and right circularly polarized light, are degenerate. However, in an external magnetic field applied parallel to the light propagation direction, the degeneration is lifted resulting from the total force (**F**) acting on the electrons that collectively oscillate in cyclotron motion:

$$\mathbf{F} = -e\mathbf{E} - e(\mathbf{v} \times \mathbf{B}) \qquad \text{(S2)}$$

where e and **v** are the charge and velocity of the electron, respectively, and **E** and **B** are external electric and magnetic field, respectively.

The difference in absorption of left and right circularly polarized light by these magnetoplasmonic modes results in derivative-shaped MCD signal (Scheme S1). The shift in frequency of the magnetoplasmonic modes ($\Delta\omega$) for a given magnetic field strength (B) relative to zero-field LSPR frequency (ω_0) is given as:

$$\Delta\omega = |\omega_B - \omega_0| = g(\omega_0)B \qquad \text{(S3)}$$

where ω_B is the frequency of the magnetoplasmonic mode (ω_B^- , ω_B^+) and $g(\omega_0) = -e/2m$ is the proportionality constant. It follows from the eq. S3 that the universal behaviors of LSPR MCD signal are linear dependence on the magnetic field and independence on temperature.

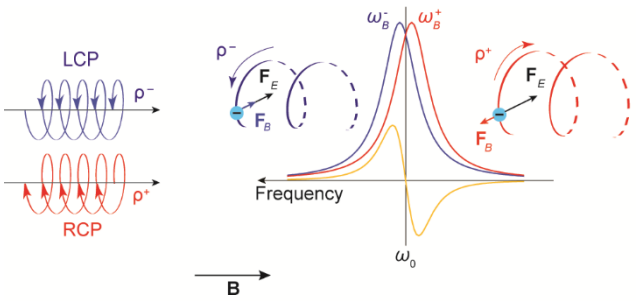

Scheme S1. Schematic representation of the origin of LSPR MCD of plasmonic NCs. The derivative-shaped MCD intensity (yellow line) is a result of the difference between the absorption of left circularly polarized light (LCP, blue line) and right circularly polarized light (RCP, red line) having ρ^- and ρ^+ helicity, respectively, for magnetic field (**B**) oriented parallel to the light propagation direction. In an external magnetic field the two degenerate LSPR modes having frequency ω_0 split, giving rise to modes with resonance frequencies ω_B^- and ω_B^+. The orientation of the magnetic component ($\mathbf{F}_B$) and electric component ($\mathbf{F}_E$) of the Lorentz force acting on free electrons, responsible for splitting of the cyclotron plasmonic modes in the magnetic field, is indicated in the scheme. A quantitative model describing the origin of magnetoplasmonic modes in nanocrystals is given in ref. 24 in the main text.

Origin of the Difference in Morphology of TiO_2 NCs. In case of TiF_4 precursor, F^- ions, formed in situ during the coordination of oleic acid to dissolved Ti^{4+}, can selectively bind to {001} facets of nucleated anatase TiO_2 nanocrystals and act as a morphology-controlling agent (ref. 30 in the main text). This selective coordination of fluoride ions hinders nanocrystal growth along {001} direction, and results in the formation of platelet-like nanocrystals. When TiF_4 and $TiCl_4$ mixture is used, the amount of HF generated during

the synthesis is significantly reduced, which leads to the formation of truncated bipyramidal nanocrystals with a relatively small surface area percentage of {001} facets, and a large percentage of {101} facets. Correspondingly, by using $TiCl_4$ precursor alone, the fraction of the {001} facets is expected to be the smallest among the three samples shown in Figure 1. It has been reported that ODOL could be used as the provider of the hydroxyl groups in non-aqueous colloidal synthesis of metal oxide NCs.[S8] The presence of ODOL as a coordinating ligand (or co-surfactant) in this synthesis can therefore accelerate the hydroxylation of Ti^{4+} in solution and the ensuing polymerization, resulting in the faster NC growth, as evident from the results in Figure 1 and Figure S4. By using a specific combination of precursors and coordinating ligands, one can systematically control the morphology and size of the TiO_2 NCs, and ultimately the formation of native defect states (see the discussion in the main text).

We note that majority of F-OLAM and M-OLAM NCs in Figures S2 and S3 appear relatively similar. The main reason for that similarity is that most F-OLAM and M-OLAM NCs are oriented along <001> direction (i.e., they rest on a {001} facet formed by truncation of the square bypiramidal NCs during their growth in solution), resulting in square projections when viewed along [001] zone axis. However, M-OLAM NCs have a significantly higher contrast, indicating a higher thickness due to lower degree of NC truncation, consistent with the nanocrystal drawing in Figure 1a (inset).

The average thickness of F-OLAM NCs are measured to be ca. 5 nm for nanoplatelets oriented perpendicular to the square base (Figure S2). On the other hand, M-OLAM samples do not show any “rod-like” features expected for nanoplatelets rotated 90 degrees relative to the square base (Figure S3). A different orientation of these non-spherical M-

OLAM NCs is the reason why some NCs appear to have a different shape in TEM images. Nevertheless, based on the large overview image (Figure S3), it is clear that these M-OLAM NCs are highly uniform in size. Importantly, using CrysTBox program analysis, we performed a detailed analysis of high resolution TEM images and the corresponding electron diffraction patterns, which allowed us to elucidate the orientation and faceting of the representative NCs (Figure 1b and Figure S1), as discussed in the manuscript. Specifically, a lower degree of truncation implies smaller fraction of {001} faceting in M-OLAM relative to F-OLAM NCs which is also well-correlated with the concentration of free electrons. Similar analysis for Cl-ODOL NCs (Figure 1b and Figure S1) revealed somewhat more complex NC faceting, but most importantly confirmed a much lower degree of truncation along <001> direction. This faceting results in elongated "rice-like" morphology of Cl-ODOL NCs, which is one of the common morphologies of TiO_2 NCs.[S9] This elongated "nanorice" morphology is also evident from the overview TEM images in Figure 1b (bottom panels), despite varying NC orientation, similarly to M-OLAM NCs. Importantly for this study, the fraction of {001} faceting is well-correlated with the concentration of charge carriers, which is ultimately enabled by fluoride ions, as discussed above. This analysis unambiguously demonstrates the correlation between the degree of truncation and a percentage of {001} plane, which is associated with plasmonic properties.

Density Functional Theory (DFT) Calculations. The electronic structure of oxygen vacancies and their role in the observed exciton splitting was also explored in more detail using DFT calculations. The electronic structure of the ideal and vacancy-doped TiO_2 supercell is shown in Figure S7. Figure S7a plots the projected density of states (PDOS) of

ideal anatase TiO_2. The valence and conduction bands have mostly oxygen 2p and titanium 3d character, respectively, as expected. The calculated band gap energy is 2.33 eV, which is in reasonable agreement with the experimental value of the optical band gap (3.2 eV), given the well-documented propensity of DFT methods to underestimate the band gap energy of semiconductors. Introduction of a single oxygen vacancy in the supercell leads to the formation of sub-band-gap states ca. 0.22 eV below the conduction band (Figure S7b and c). These states have Ti 3d character, and are associated with the formation of Ti^{3+}. These results are consistent with the premise that oxygen vacancies can act as trap states which foster the reduction of the Ti^{4+} host lattice cations and the subsequent Ti^{3+} self-doping. The introduction of oxygen vacancy also shifts the Fermi level to higher energies, associated with the formation of electron donor states. The formation of shallow Ti^{3+} states near the conduction band edge can explain that the individual Ti^{3+} centers and complexes involving exchange-coupled Ti^{3+} contribute to the observed band splitting in addition to magnetoplasmonic modes.

SUPPORTING REFERENCES

(S1) Gordon, T. R.; Cargnello, M.; Paik, T.; Mangolini, F.; Weber, R. T.; Fornasiero, P.; Murray, C. B. Nonaqueous Synthesis of TiO_2 Nanocrystals Using TiF_4 to Engineer Morphology, Oxygen Vacancy Concentration, and Photocatalytic Activity. *J. Am. Chem. Soc.* **2012**, *134*, 6751-6761.

(S2) Yin, P.; Tan, Y.; Fang, H.; Hegde, M.; Radovanovic, P. V. Plasmon-Induced Carrier Polarization in Semiconductor Nanocrystals. *Nat. Nanotechnol.* **2018**, *13*, 463-467.

(S3) Yin, P.; Hegde, M.; Tan, Y.; Chen, S.; Garnet, N.; Radovanovic, P. V. Controlling the Mechanism of Excitonic Splitting in In_2O_3 Nanocrystals by Carrier Delocalization. *ACS Nano* **2018**, *12*, 11211-11218.

(S4) Giannozzi, P.; Baroni, S.; Bonini, N.; Calandra, M.; Car, R.; Cavazzoni, C.; Ceresoli, D.; Chiarotti, G. L.; Cococcioni, M.; Dabo, I.; Dal Corso, A.; de Gironcoli, S.; Fabris, S.; Fratesi, G.; Gebauer, R.; Gerstmann, U.; Gougoussis, C.; Kokalj, A.; Lazzeri, M.; Martin-Samos, L.; Marzari, N.; Mauri, F.; Mazzarello, R.; Paolini, S.; Pasquarello, A.; Paulatto, L.; Sbraccia, C.; Scandolo, S.; Sclauzero, G.; Seitsonen, A. P.; Smogunov, A.; Umari, P.; Wentzcovitch, R. M. Quantum ESPRESSO: a Modular and Open-Source Software Project for Quantum Simulations of Materials. *J. Phys.: Condens. Matter.* **2009**, *21*, 395502.

(S5) Mattioli, G.; Alippi, P.; Filippone, F.; Caminiti, R.; Amore Bonapasta, A. Deep versus Shallow Behavior of Intrinsic Defects in Rutile and Anatase TiO_2 Polymorphs. *J. Phys. Chem. C* **2010**, *114*, 21694-21704.

(S6) Mattioli, G.; Amore Bonapasta, A.; Bovi, D.; Giannozzi, P. Photocatalytic and Photovoltaic Properties of TiO_2 Nanoparticles Investigated by *Ab Initio* Simulations. *J. Phys. Chem. C* **2014**, *118*, 29928-29942.

(S7) Kumar Sahoo, P.; Kamal, S.; Premkumar, M.; Jagadeesh Kumar, T.; Bojja, S.; Singh, A. K.; K. Srivastava, S.; Chandra Sekhar, K., Synthesis of Tungsten Nanoparticles by Solvothermal Decomposition of Tungsten Hexacarbonyl. *Int. J. Refract. Met. Hard Mater.* **2009,** *27*, 784-791.

(S8). Cao, S.; Zhang, S.; Zhang, T.; Fisher, A.; Lee, J. Y., Metal-Doped TiO_2 Colloidal Nanocrystals with Broadly Tunable Plasmon Resonance Absorption. *J. Mater. Chem. C* **2018,** *6*, 4007-4014.

(S9) Wen, C. Z.; Jiang, H. B.; Qiao, S. Z.; Yang, H. G.; Lu, G. Q. Synthesis of High-Reactive Facets Dominated Anatase TiO_2. *J. Mater. Chem.* **2011**, *21*, 7052-7061.